Supporting Information for

Versatile nickel-tungsten bimetallics/carbon nanofiber catalysts for direct conversion of cellulose to ethylene glycol

Ying Yang,* Wen Zhang, Feng Yang, Dennis E. Brown, Yang Ren, Sungsik Lee, Dehong Zeng, Qiang Gao and Xin Zhang

Corresponding Author

E-mail: catalyticscience@163.com

1 Chemicals and reagents

All chemicals are commercially received and used without any further purification. Zinc acetate dehydrate ($Zn(Ac)\cdot 2H_2O$, AR), sodium tungstate dihydrate ($Na_2WO_4\cdot 2H_2O$, AR), nickel chloride hexahydrate ($NiCl_2\cdot 6H_2O$, AR), trimesic acid ($C_9H_6O_6$, > 98%, TCI), N,N-dimethylformamide (DMF, AR), cellulose microcrystalline ($(C_6H_{10}O_5)_n$), ethylene glycol ($C_2H_6O_2$, AR), 1,2-propylene glycol ($C_3H_8O_2$, AR), erythritol ($C_4H_{10}O_4$, 99%, aladdin), sorbitol ($C_6H_{14}O_6$, BR), mannitol ($C_6H_{14}O_6$, AR), acetonitrile (C_2H_3N, HPLC, sigma), nitrogen (N_2, > 99.999%), hydrogen (> 99.999%), and ethanol (C_2H_6O, AR).

2 Characterization

Powder XRD was collected with a Bruker D8 Advance X-ray diffractometer with nickel filtered CuKα radiation (λ = 1.5406 Å). The samples were scanned in the 2θ range of 5-80^o and in steps of 4 ^{o}/min. The infrared spectra of samples were recorded in KBr disks using a Nicolet Nexus 870 FTIR spectrometer. SEM analysis was performed on a FEI-Quanta 200F field-emission scanning microscope operated at 15 kV with an EDS detector to determine the morphology of the prepared samples. The TEM images, high-resolution TEM images, and micro electron diffraction were analyzed using a FEI Tecnai G2 F20 transmission electron microscope equipped with an energy dispersive X-ray spectroscopic analyzer operated at a voltage of 200 kV. Samples were sonicated for 5 min in EtOH, one drop of the suspended sample was dripped in a holely carbon microgrid supported on a 300 mesh copper grid. The histograms of metal particle sizes were established from the measurement of 200 particles. N_2 adsorption/desorption isotherms were recorded at 77 K using a JW-BK222 static volumetric gas adsorption instrument manufactured by Beijing JWCB Sci. & Tech. Co., Ltd. Before measurements, the samples were de-gassed at 300 ^{o}C for 3 h in vacuum. Specific surface area was determined by the Brunauer-Emmett-Teller (BET) method and mesopore size distributions were measured by using the Barrett-Joyner-Halenda (BJH) method from the desorption branch of the isotherms. The linearized BET model was used to fit the microporous data within the relative pressure range of $0.001 < P/P_0 < 0.05$. The micropore size distributions were determined by using the Horvath-Kawazoe (H-K) method

assuming slit pore geometry. *In situ* high-energy synchrontron X-ray diffraction measurements were performed at the 11-ID-C beamline of the Advanced Photon Source (APS) at Argonne National Laboratory. X-rays of 115 keV energy and 0.6 mm × 0.6 mm beam size were used to obtain two-dimensional (2D) diffraction patterns in the transmission geometry using a Perkin-Elmer large area detector placed at 1.6 m from the sample. X-ray absorption fine structure (XAFS) was carried out on the 12-BM-B beamline of APS at Argonne National Laboratory. The XAFS data were obtained in the fluorescence mode at the Ni K-edge (8333.0 eV) and W L_2-edge (11544.0 eV), and using Ni foil and Pt foil as the reference, respectively. W L_2-edge scan was employed and Pt foil was used as a reference because there is a serious energy overlap between the Ni K-edge and fluorescence lines of W L_3-edge. The XAFS data were processed using the Athena software for background removal, post-edge normalization and X-ray absorption near edge structure (XANES) analysis. The oxidation states of the samples were determined by comparing the inflection point of the edge from the sample to that of standards with known oxidation state. The extended X-ray absorption fine structure (EXAFS) was analyzed using Artemis software, which implemented FEFF. The EXAFS data reduction was conducted by utilizing the standard procedures. The EXAFS function, χ, was obtained by subtracting the *post*-edge background from the overall absorption and then normalized with respect to the edge jump step. Subsequently, k^3-weighted $\chi(k)$ data in k space were Fourier transformed to r space to separate the EXAFS contributions from the different coordination shells. However, fitting Ni and W local structure doesn't have physical solution, and the error of coordination numbers is always larger than 10%. Therefore, the fitted parameters were not listed and discussed in this study.

Ni and W content was estimated by inductively coupled plasma-atomic emission spectroscopy (ICP-AES) analysis conducted on a Perkin Elmer emission spectrometer. Certain amount of vacuum-dried material was placed in a digester with PTFE lined, and dissolved in 4 mL of aqua fortis solution mixed with 1 mL H_2O_2. Microwave digestion was carried out for 10 min to completely dissolve the metal species. After cooling, each solution was filtered through a 0.45 μm polyethersulfone filter and then submitted for analysis.

Table S1 Gas product distribution using different catalysts.

Entry	Materials	Yield (%)				
		CO	CO_2	CH_4	C_2H_6	C_3H_8
1	$Ni_{0.3}$-$W_{0.3}$/CNF	2.3	20.2	4.5	1.0	-
2	$Ni_{0.6}$-W_0/CNF	10.2	28.9	15.2	4.3	2.6
3	$Ni_{0.5}$-$W_{0.1}$/CNF	8.3	23.0	6.8	3.7	1.0
4	$Ni_{0.4}$-$W_{0.2}$/CNF	1.4	18.0	10.9	2.8	-
5	$Ni_{0.2}$-$W_{0.4}$/CNF	1.2	18.9	5.6	4.7	3.6
6	$Ni_{0.1}$-$W_{0.5}$/CNF	4.2	12.0	4.2	0.8	-
7	Ni_0-$W_{0.6}$/CNF	3.6	6.5	1.3	0.6	-

Reaction conditions: 0.5 g cellulose, 0.15 g catalyst, 30 mL H_2O, 6.0 MPa H_2 pressure (measured at room temperature) and at 245 ^oC.

Table S2 Metal loading and textural property of various $Ni_{0.6-x}$-W_x/CNF catalysts

Materials	Theoretical W/Ni molar ratio	Ni content (wt%)	W content (wt%)	Estimated W/Ni molar ratio	BET surface area[a] (m^2 g^{-1})	Pore size[b] (nm)	Pore volume (cm^3 g^{-1})
$Ni_{0.5}$-$W_{0.1}$/CNF	1/5	1.81	0.03	0.006	1727	3.6	1.40
$Ni_{0.4}$-$W_{0.2}$/CNF	2/4	2.08	0.02	0.003	1019	3.7	0.81
$Ni_{0.3}$-$W_{0.3}$/CNF	3/3	0.37	0.06	0.051	848	3.8	0.87
$Ni_{0.2}$-$W_{0.4}$/CNF	4/2	0.94	0.04	0.012	822	3.9	0.71
$Ni_{0.1}$-$W_{0.5}$/CNF	5/1	0.52	0.01	0.070	746	3.7	0.75
Spent $Ni_{0.3}$-$W_{0.3}$/CNF					167	3.6	0.27

[a]The BET surface areas were obtained from the adsorption branches in the relative pressure range of 0.05-0.20.

[b]The pore size distributions were calculated from the desorption branches by the Barret-Joyner-Halenda (BJH) method.

Table S3 Comparison of various tungstenic catalysts

Materials	Catalyst amount (g)	Cellulose amount (g)	W content (wt%)	EG yield (%)	Productivity ($mol_{EG}h^{-1}g_W^{-1}$)	Reference
WC_x/MC	0.30	1.0	42	72.9	0.187	(4)
2%Ni-30%W_2C/AC-973	0.15	0.5	30	61.0	0.219	(3)
Ni5-W15/SBA-15	0.30	1.0	15	76.1	0.546	(5)
2%Ni-30%W_2C/AC	0.15	0.5	30	55.3	0.198	(8)
0.5%WO_3/C	0.016 g WO_3	1.0	79	5.2	0.131	(6)
50%WO_3/ZrO_2	0.016 g WO_3	1.0	79	7.0	0.178	(6)
36%WO_3/TiO_2	0.016 g WO_3	1.0	79	7.5	0.190	(6)
50%WO_3/Al_2O_3	0.016 g WO_3	1.0	79	9.7	0.246	(6)
50%WO_3/Al_2O_3+C_{act}	0.016 g WO_3	1.0	79	5.9	0.149	(6)
WO_3	1 g WO_3	1.0	79	48.9	0.020	(6)
50%WO_3/Al_2O_3+C_{act}	0.016 g WO_3	1.0	79	16.6	0.422	(6)
12%WO_3/TiO_2	0.016 g WO_3	1.0	79	8.7	0.221	(6)
WO_2	1 g WO_2	1.0	85	8.5	0.003	(6)
W	1 g W	1.0	100	4.1	0.001	(6)
W_2C	1 g W_2C	1.0	97	11.5	0.004	(6)
$Ni_{0.5}$-$W_{0.1}$/CNF	0.15	0.5	0.0332	28.7	23.27	this study
$Ni_{0.4}$-$W_{0.2}$/CNF	0.15	0.5	0.0176	30.2	46.13	this study
$Ni_{0.3}$-$W_{0.3}$/CNF	0.15	0.5	0.0590	33.6	15.31	this study
$Ni_{0.2}$-$W_{0.4}$/CNF	0.15	0.5	0.0359	27.6	20.66	this study
$Ni_{0.1}$-$W_{0.5}$/CNF	0.15	0.5	0.0113	29.8	70.85	this study

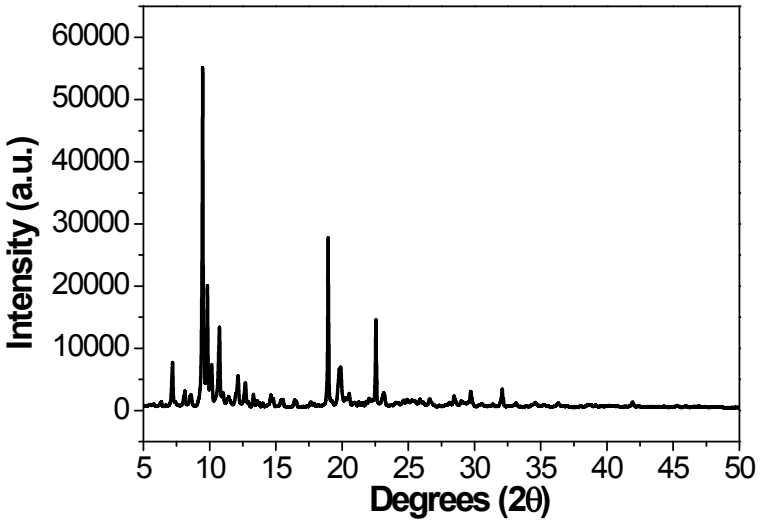

Fig. S1 XRD pattern of $Ni_{0.3}$-$W_{0.3}$-ZnBTC.

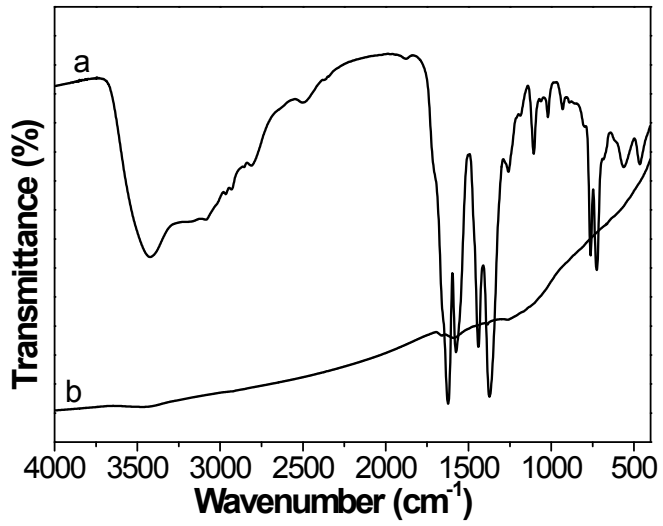

Fig. S2 FT-IR spectra of (a) $Ni_{0.3}$-$W_{0.3}$-ZnBTC and (b) $Ni_{0.3}$-$W_{0.3}$/CNF.

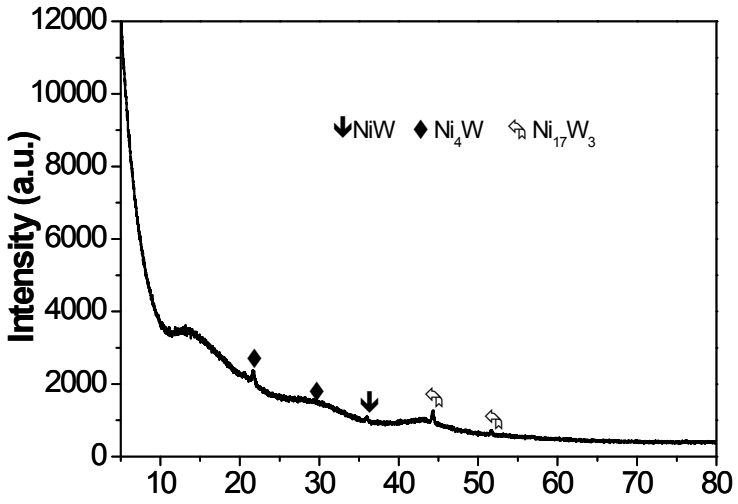

Fig. S3 XRD pattern of $Ni_{0.3}$-$W_{0.3}$/CNF.

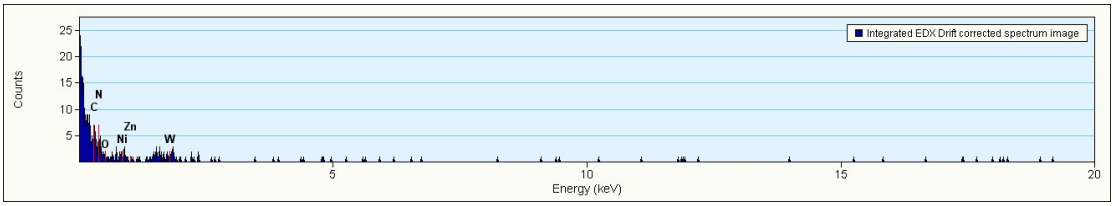

Fig. S4 TEM-EDX results for $Ni_{0.3}$-$W_{0.3}$/CNF.

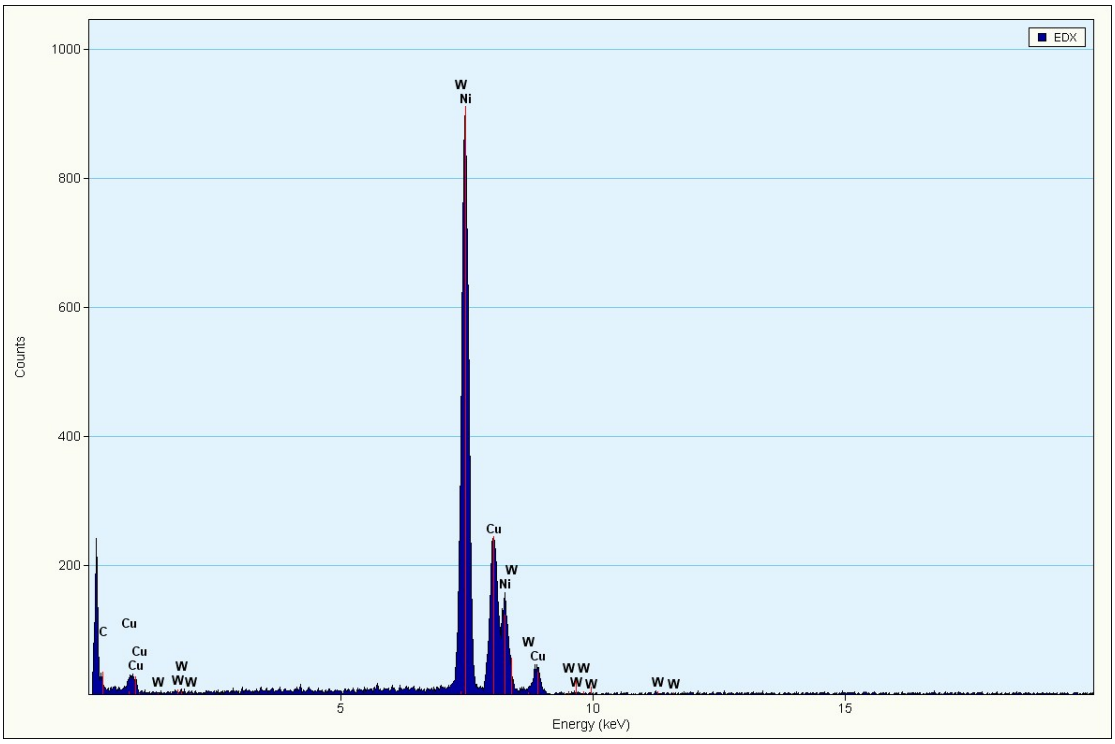

Fig. S5 TEM-EDX results for a single particle in $Ni_{0.3}$-$W_{0.3}$/CNF.

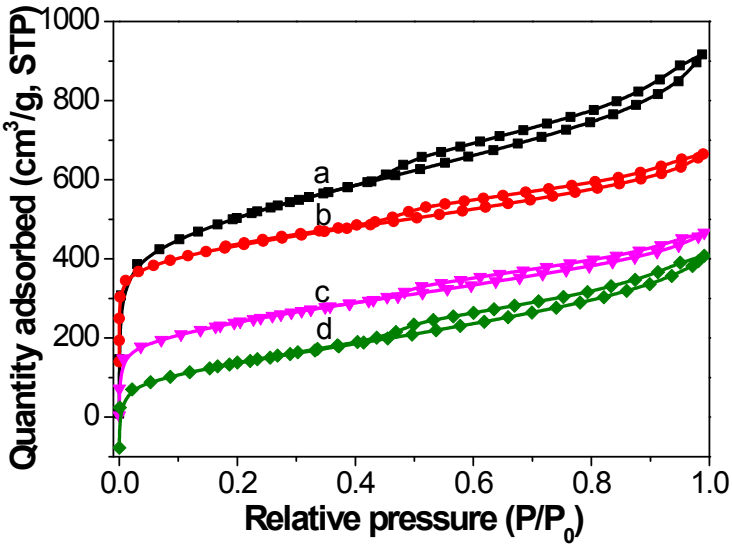

Fig. S6 N_2 adsorption/desorption isotherms of (a) $Ni_{0.5}$-$W_{0.1}$/CNF, (b) $Ni_{0.4}$-$W_{0.2}$/CNF, (c) $Ni_{0.2}$-$W_{0.4}$/CNF, and (d) $Ni_{0.1}$-$W_{0.5}$/CNF.

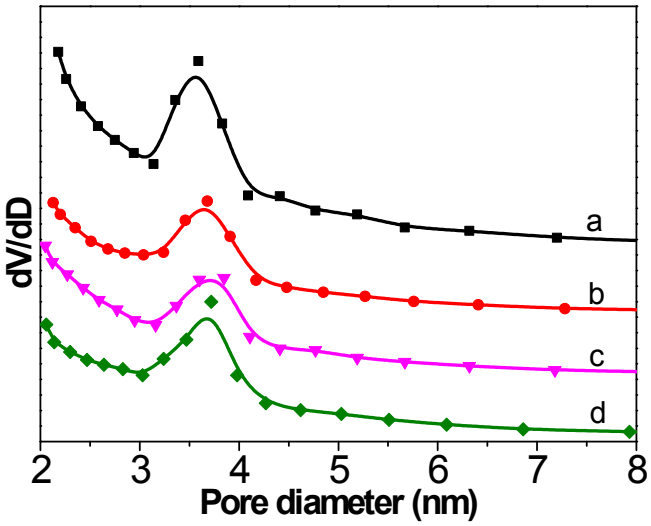

Fig. S7 Mesopore size distribution curves of (a) $Ni_{0.5}$-$W_{0.1}$/CNF, (b) $Ni_{0.4}$-$W_{0.2}$/CNF, (c) $Ni_{0.2}$-$W_{0.4}$/CNF, and (d) $Ni_{0.1}$-$W_{0.5}$/CNF.

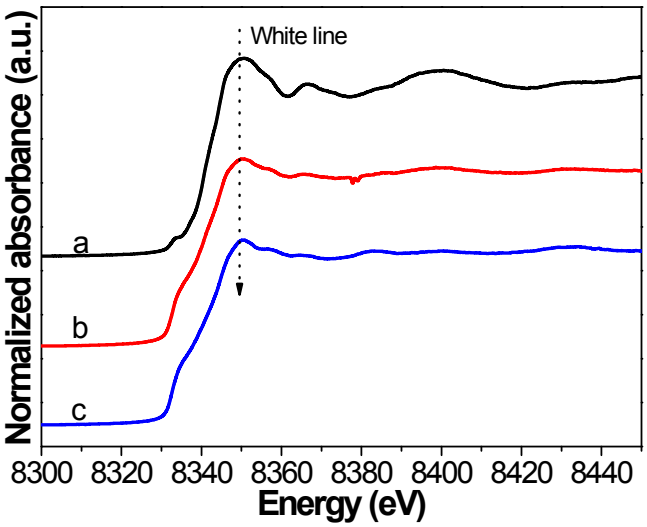

Fig. S8 Ni K-edge XANES of (a) $Ni_{0.5}$-$W_{0.1}$/CNF, (b) $Ni_{0.2}$-$W_{0.4}$/CNF, and (c) $Ni_{0.1}$-$W_{0.5}$/CNF.

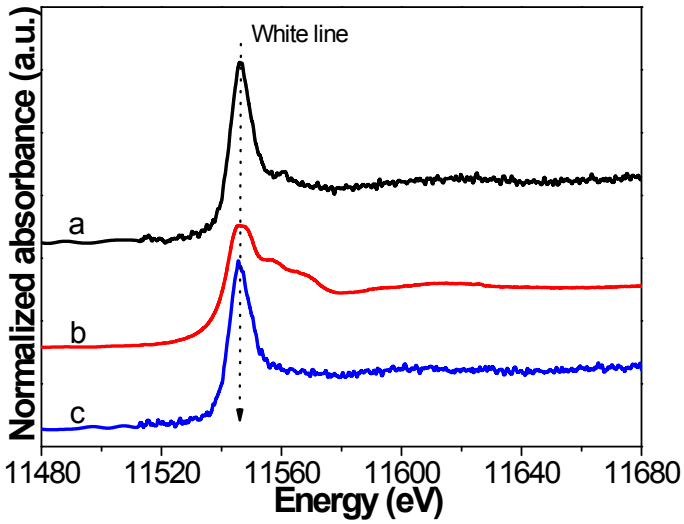

Fig. S9 W L_2-edge XANES of (a) $Ni_{0.5}$-$W_{0.1}$/CNF, (b) $Ni_{0.2}$-$W_{0.4}$/CNF, and (c) $Ni_{0.1}$-$W_{0.5}$/CNF.

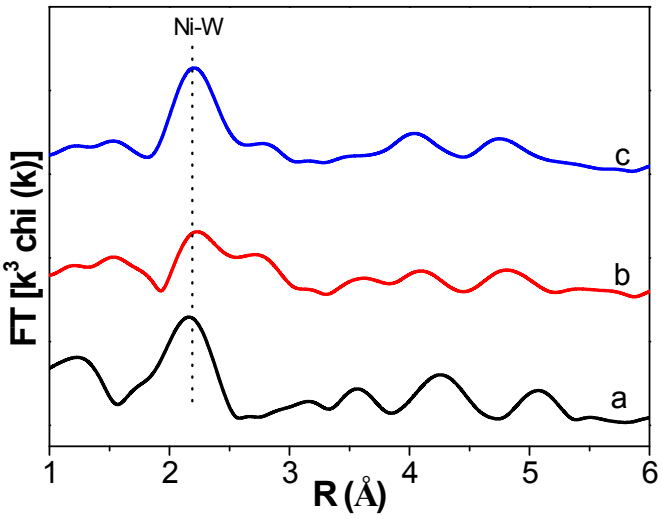

Fig. S10 Ni K-edge EXAFS of (a) $Ni_{0.5}$-$W_{0.1}$/CNF, (b) $Ni_{0.2}$-$W_{0.4}$/CNF, and (c) $Ni_{0.1}$-$W_{0.5}$/CNF.

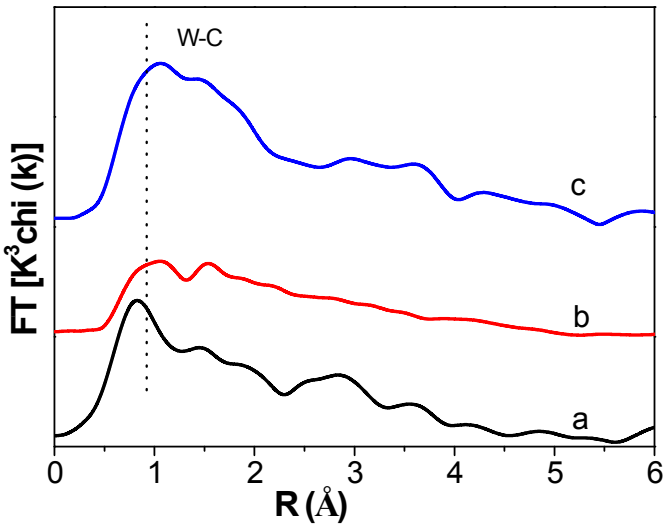

Fig. S11 W L_2-edge EXAFS of (a) $Ni_{0.5}$-$W_{0.1}$/CNF, (b) $Ni_{0.2}$-$W_{0.4}$/CNF, and (c) $Ni_{0.1}$-$W_{0.5}$/CNF.

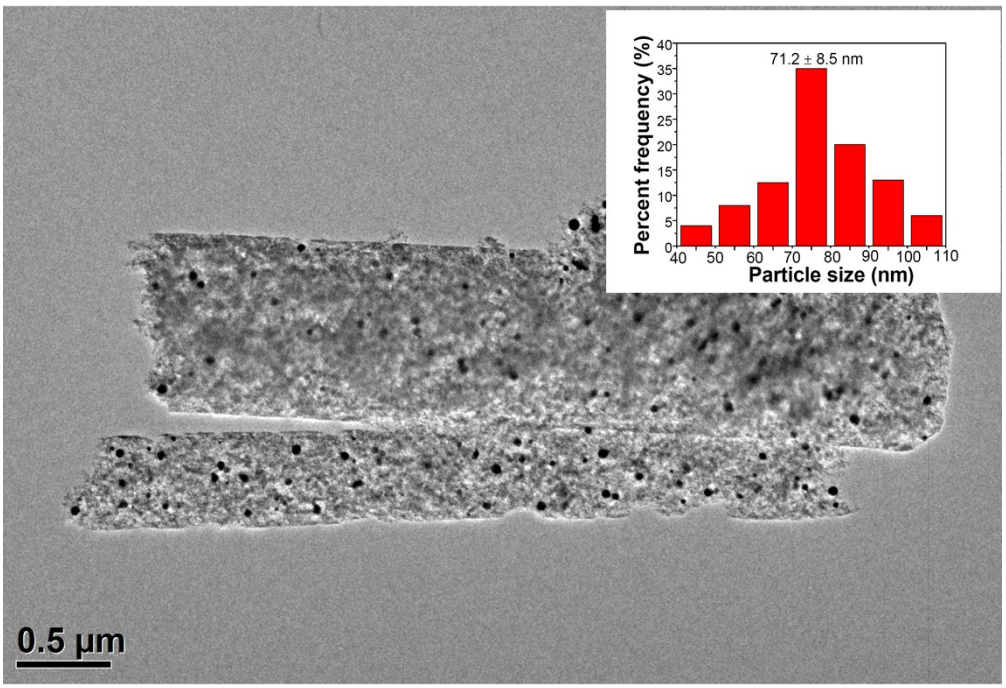

Fig. S12 TEM image and the corresponding particle size distribution histogram (inset) of spent $Ni_{0.3}$-$W_{0.3}$/CNF.

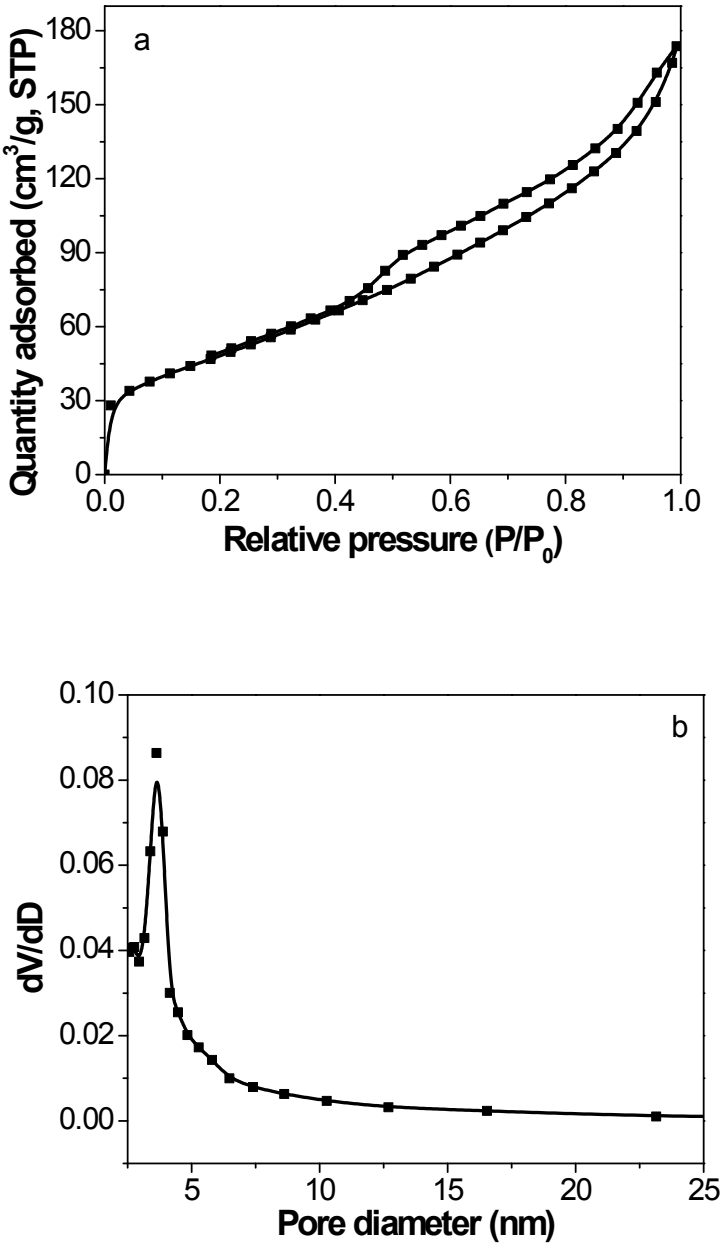

Fig. S13 N_2 adsorption/desorption isotherm (a) and the corresponding pore size distribution curve (b) of spent $Ni_{0.3}$-$W_{0.3}$/CNF.